



Subject Areas:

Computer modelling and simulation,
Fluid mechanics

Keywords:

Self-folding, three-phase simulation,
micro-origami, fluid-structure
interaction.

Author for correspondence:

Gregory Lecrivain

e-mail: g@lecrivain.hzdr.de

Self-folding of two-dimensional thin templates into pyramidal micro-structures by a liquid drop - a numerical model

Gregory Lecrivain¹, Pierre Lorenz², Klaus Zimmer³ and Uwe Hampel⁴

¹Helmholtz-Zentrum Dresden-Rossendorf, Institut für Fluidodynamik, Bautzner Landstraße 400, 01328 Dresden, Germany

²Leibniz-Institut für Oberflächenmodifizierung e.V., Permoserstraße 15, 04315 Leipzig, Germany

³Leibniz-Institut für Oberflächenmodifizierung e.V., Permoserstraße 15, 04315 Leipzig, Germany

⁴Technische Universität Dresden, Institut für Energietechnik, Professur für Bildgebende Messverfahren für die Energie- und Verfahrenstechnik, Dresden, Germany

We present a numerical framework bringing together a structural and a surface-energy minimization model to compute nano- and micro-origami self-folding processes, that are three-dimensional in nature. A liquid drop, initially at rest on the template, triggers the spontaneous folding and deforms dynamically with the template. As application, the self-folding of thin two-dimensional templates into pyramidal micro-structures is simulated. Each template is composed of a fixed regular base connected to rigid triangular sides by two elastic hinges. We presently determine the condition, at which the transition from partial to full drop encapsulation occurs. The present model has many advantages. It does not depend on arbitrary user-defined parameters and addresses unsteady dynamics by incorporating time-derivative terms.

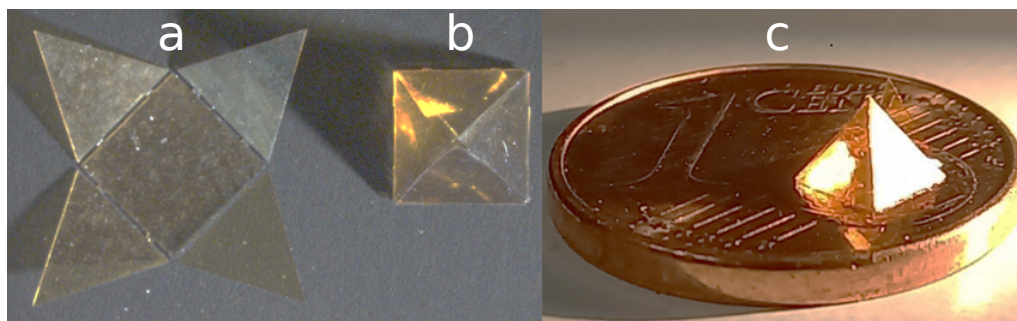


Figure 1. Using a liquid drop, the unfolded two-dimensional template (a), called a structural net, spontaneously turns into a pyramidal micro-structure (b-c). Hinges, connecting the base to each triangular side, deform during the folding. Eventually, the drop is fully encapsulated. The experiment was performed for illustration purposes.

1. Introduction

Capillary-induced nano and micro-origami are processes, by which surface tension spontaneously folds a thin planar template into a hollow three-dimensional structure [1–5]. In nature, petaloid flowers have developed self-folding properties, that are solely triggered by surface tension [6]. In nano and micro-engineering involving thin film planar technology [7–9], three-dimensional structures have been produced by depositing a liquid drop onto a thin and foldable two-dimensional polymer template. Figure 1 illustrates a pyramidal microstructure, that we obtained by placing a drop onto a specific thin planar template, specifically referred to as structural “net” in the technical literature [10–12]. Elastic hinges, connecting each triangular side of the net to the rectangular base, hold the template together. The liquid drop, by minimizing its contact surface to the ambient air, triggers large deformation of the hinges and hence the folding. By appropriately tailoring the structural net, the final folded structure remains three-dimensional after the drop fully evaporates [13]. Inspired by that, micro-origami has found further application in biomedicine, for example, in the selective encapsulation of cells and bacteria by functionalizing the surfaces of a foldable template [14–16]. The simulation of nano and micro-origami is challenging. Strong structural deformation, moving contact line, drop affinity to the template along with water evaporation should ideally be taken into account. A number of models have been suggested in the past. Patra et al. [17] used molecular dynamics to simulate the capillary folding of a graphene petal-like structural net by a nano-drop. In their three-dimensional simulation, thousands of water molecules were used to discretize the nano-drop. Leong et al. [18] performed quasi-static simulations with the Surface Evolver [19] to simulate the capillary folding of structural nets into micro-cubes. The structural nets were made of thin square plates connected to one another by deformable hinges. In their work, the Surface Evolver was used to iteratively re-distribute the nodes of the drop surface by minimizing its surface energy. Similarly, in [20,21], the authors investigated the fabrication of five-faced micro-cubes. By deliberately omitting the top surface of the micro-cube, the volume of water could be greater than that of the closed micro-cube. In their work, a two-dimensional variational approach was used. The total energy, that is the sum of a bending energy associated with the hinge deformation and an interfacial energy associated with the drop deformation, is minimized. To model the hinge, a dimensionless parameter was introduced. It characterizes the ratio of the reference bending force to the surface tension force. Further models based on the variational approach have been suggested for the general simulation of elasto-capillary deformations [22–24]. In [25], equilibrium solutions were derived for a two-dimensional drop resting on an elastic beam. Self-encapsulation by an elastic rod was also studied experimentally and numerically in [26]. Brubaker et al. [27] are one of the few groups to have

attempted to simulate the three-dimensional folding of a flexible thin template by a drop. Their three-dimensional extension, described as highly challenging by the authors, was however only valid for small deformations and could not accurately capture the full encapsulation of the drop. Most of the numerical models presented in the literature and describing the template folding and the drop deformation in a dynamic way are two-dimensional. Three-dimensional extensions exist. Yet, they are either limited to small deformations or reductive. It is often assumed, that the drop takes the shape of a spherical cap throughout the folding process [24,27]. Here, an alternative method is proposed to simulate the three-dimensional folding of a structural net composed of thin plates, which are connected to one another by elastic hinges. As academic application, star-like structural nets are chosen because they are reminiscent of those presented in [18,20,21]. In their final states, the folded micro-structures take pyramidal shapes.

This manuscript is arranged as follows. In the methods, we first begin by describing the hinge model. Second, we describe the drop deformation model based on the minimization of a free energy. The dynamic coupling between the two models is then addressed by providing a numerical description for the calculation of the surface tension force. In the results, we showcase the self-folding of the star-like structural nets into micro-pyramids and determine the necessary condition triggering a full encapsulation of the drop, as experimentally illustrated in Figure 1b-c.

2. Methods

At simulation start, the structural nets are unfolded pyramidal micro-structures with a regular polygonal base composed of $N = 3, 4, 5, 6$ and 7 triangular sides. A greater number of sides is possible. The base is fixed and connects to each triangular side by two deformable hinges. Figure 2 shows some selected structural nets, on which the drop initially rests. With a zero hinge length, the volume $\mathcal{V} = \mathcal{A}h/3$ of each pyramid is identical. The base area \mathcal{A} and the height h of each pyramid are hence identical too and are set to $\mathcal{V} = V_0$ and $h = 4.1R_0$, where V_0 is the drop volume and R_0 the equivalent drop radius. Considering a hemisphere as equivalent drop geometry, the equivalent radius is given by $V_0 = 2/3\pi R_0^3$. With a the apothem of the polygonal base, s and b the base and height of each triangular side, the length parameters of each unfolded structural net are given by

$$a^2 = \frac{\mathcal{A}}{N} \cot\left(\frac{\pi}{N}\right), \quad (2.1)$$

$$s^2 = 4\frac{\mathcal{A}}{N} \tan\left(\frac{\pi}{N}\right), \quad (2.2)$$

$$b^2 = h^2 + a^2. \quad (2.3)$$

The distance separating the base to each triangular side, which is equal to the hinge length, is set to $\ell/R_0 = 0.164$. In the simulation, each base and triangular side are arbitrarily thin prisms represented by a triangulated surface mesh. In accordance with computer graphics [28], each surface mesh is described by an array of vertices and triangular faces.

(a) Hinges

To simulate the hinge deformation, the cohesive beam model [30] derived analytically from the Euler-Bernoulli beam theory [31] is here used. Because the hinge model is already presented in the author's previous work [32], we focus here on its most salient features. Each hinge is discretized into a chain of N_b spherical beads with identical radii r_b . As illustrated in Figure 3, the first bead with index $i = 0$ is connected to the base and the last one to the triangular side. The trajectory of each bead is computed independently as

$$\frac{d\mathbf{X}_i}{dt} = \mathbf{V}_i, \quad (2.4)$$

$$\frac{d\mathbf{Q}_i}{dt} = \frac{1}{2}\mathbf{A}_i \cdot \mathbf{Q}_i, \quad (2.5)$$

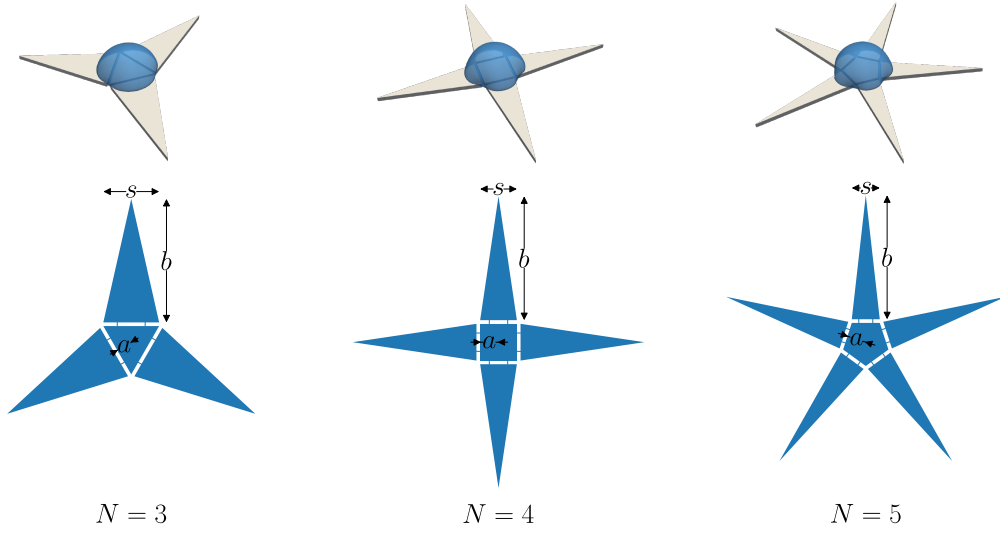


Figure 2. Unfolded pyramidal micro-structures, or structural nets. a , s and b are the base apothem, the side length and the side height. Each side is connected to the base by two deformable hinges. Using the marching cubes [29], the drop is conveniently represented by a three-dimensional surface mesh.

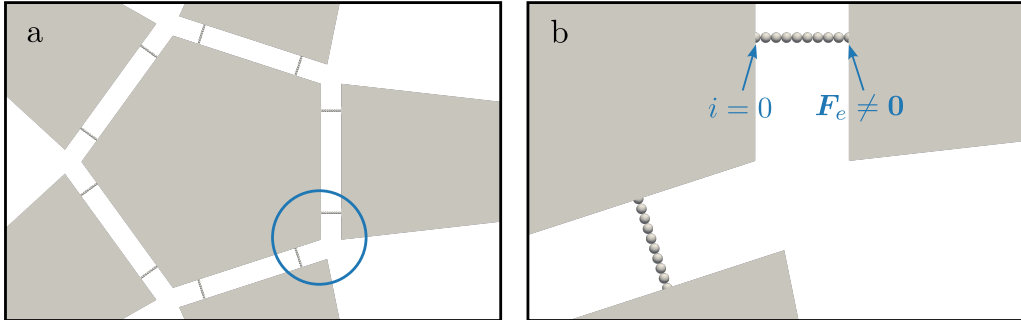


Figure 3. Each hinge is decomposed into $N_b = 10$ spherical beads. The first bead, associated with the index $i = 0$, is fixed to the base. The external force only acts on the last bead, to which the triangular side is attached.

where \mathbf{X}_i is the position of i -th bead centre of mass, $\mathbf{Q}_i = (Q_s \ Q_x \ Q_y \ Q_z)_i^\top$ the quaternion associated with the angular position of the bead, $(Q_s)_i$ and $(Q_x \ Q_y \ Q_z)_i^\top$ the scalar and vector parts of the quaternion, \mathbf{V}_i and $\boldsymbol{\Omega}_i = (\Omega_x \ \Omega_y \ \Omega_z)_i^\top$ the translational and rotational velocities and \mathbf{A}_i a 4×4 orthogonal matrix given by

$$\mathbf{A}_i = \begin{pmatrix} 0 & -\Omega_x & -\Omega_y & -\Omega_z \\ \Omega_x & 0 & -\Omega_z & \Omega_y \\ \Omega_y & \Omega_z & 0 & -\Omega_x \\ \Omega_z & -\Omega_y & \Omega_x & 0 \end{pmatrix}_i. \quad (2.6)$$

The dot operator in Equation 2.5 denotes the product $A_{ij}Q_j$ used in the conventional ij-matrix notation. Each bead interacts with its next consecutive neighbor by a virtual beam. At each

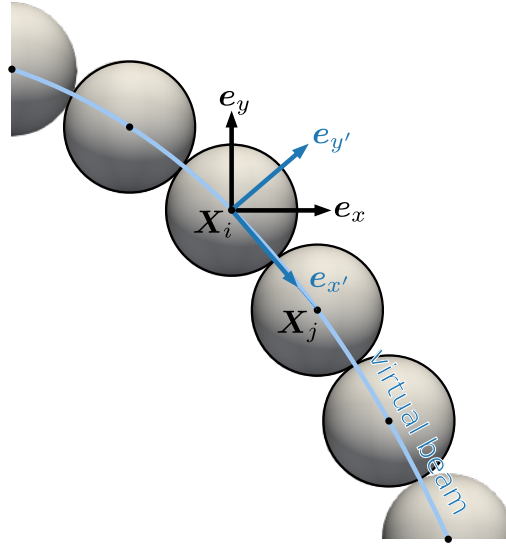


Figure 4. A bead interacts with its direct neighbors via structural forces derived from the elastica theory. the structural forces are conveniently expressed in the local beam frame $(\mathbf{X}_i \mathbf{e}_{x'} \mathbf{e}_{y'} \mathbf{e}_{z'})$.

extremity of the virtual beam, a structural force \mathbf{F}_b and torque \mathbf{T}_b are exerted on the i -th bead and its next neighbor, the j -th bead, where $j = i + 1$. With these structural forces yet to be formulated, the velocities of each bead are given by

$$m_b \left(\frac{d\mathbf{V}_i}{dt} + \frac{\mathbf{V}_i}{\tau_b} \right) = (\mathbf{F}_b)_i + \mathbf{F}_e, \quad (2.7)$$

$$\mathbf{I}_b \cdot \left(\frac{d\boldsymbol{\Omega}_i}{dt} + \frac{\boldsymbol{\Omega}_i}{\tau_b} \right) = (\mathbf{T}_b)_i + \mathbf{T}_e, \quad (2.8)$$

where m_b is the bead mass, \mathbf{I}_b a diagonal matrix whose components are the bead inertia moments, τ_b a response time accounting for material damping [33], \mathbf{F}_e and \mathbf{T}_e external force and torque associated with the surface tension. In this work, \mathbf{F}_e and \mathbf{T}_e only act on the last bead of the hinge. In the beam model, the structural forces $(\mathbf{F}_b)_i$ and $(\mathbf{F}_b)_j$ are conveniently expressed in the local beam frame $(\mathbf{X}_i \mathbf{e}_{x'} \mathbf{e}_{y'} \mathbf{e}_{z'})$ (See Figure 4). The unit vector defined in the axial beam direction is given by $\mathbf{e}_{x'} = (\mathbf{X}_j - \mathbf{X}_i) / |\mathbf{X}_j - \mathbf{X}_i|$. The corresponding component of the structural force acting on the i -th and j -th beads are given by

$$(\mathbf{F}_b \cdot \mathbf{e}_{x'})_i = \frac{\pi E r_b}{2} (|\mathbf{X}_j - \mathbf{X}_i| - 2r_b), \quad (2.9)$$

$$(\mathbf{F}_b \cdot \mathbf{e}_{x'})_j = -(\mathbf{F}_b \cdot \mathbf{e}_{x'})_i, \quad (2.10)$$

where E is the Young modulus with respect to the hinge material. The other two force components acting in the tangential beam directions along with the torques are formulated in [32], whereby a similar notation has purposely been used here. The bead position and quaternion are integrated in time via an explicit first-order forward method and velocities via an explicit second-order Adams-Bashforth method. We define the reference structural force associated with the hinge as

$$F_s = \frac{EI}{\ell^2}, \quad (2.11)$$

where $I = \pi r_b^4 / 4$ is the area moment of inertia and $\ell = 2r_b(N_b - 1)$ the hinge length.

(b) Drop

The liquid drop, the ambient gas and the structural net are replaced with continuous concentration fields $\phi_\ell(\mathbf{x}, t)$, $\phi_g(\mathbf{x}, t)$ and $\phi_s(\mathbf{x}, t)$, where $\mathbf{x} = (x y z)^\top$ is a point in space and t the time. The hinge is here left out because it is spatially too small to be considered a field. As one moves from the inner to the outer phase region, each concentration field smoothly varies from unity to zero over an interfacial width ξ . The drop shape is a-priori unknown. Hence, a modified Allen-Cahn model [34], that relies on the minimization of a free energy $E(\phi, \nabla\phi)$ following the Ginzburg–Landau theory [35], is here employed. Dropping the subscript associated with the liquid for better readability, that is $\phi = \phi_\ell$, the spacial and temporal evolution of the liquid concentration is obtained by solving

$$\frac{\partial\phi}{\partial t} + \mathbf{u} \cdot \nabla\phi = -\frac{1}{\tau_d} \frac{\delta E}{\delta\phi}, \quad (2.12)$$

where \mathbf{u} is an Eulerian velocity field associated with the folding of the structural net and τ_d a response time associated with the mobility of the drop. The advection term $\mathbf{u} \cdot \nabla\phi$ on the left-hand side of Equation 2.12 contributes to a change in the drop shape caused by the displacement of each triangular side, while the right-hand side term strives for an energetically stable drop shape. The functional derivative of the free energy is suggested as

$$\frac{\delta E}{\delta\phi} = f_b(\phi) - \xi^2 \nabla^2 \phi + f_\ell(\phi, \phi_g, \phi_s) + f_w(\phi, \phi_s, \gamma), \quad (2.13)$$

where f_b is a bulk term, $-\xi^2 \nabla^2 \phi$ an interfacial term addressing the smooth transition from unity to zero across the interface, f_ℓ a Lagrangian multiplier, f_w a wall correction term accounting for the drop affinity to the template and γ the contact angle. The bulk term, derived from a double-well potential having two local minima located at $\phi = 0$ and $\phi = 1$, is given by

$$f_b = 4\phi(\phi - 1)(\phi - \phi_c), \quad (2.14)$$

where $\phi_c = 1/2 + \beta(V_t/V_0 - 1)$ is a corrected term maintaining the constant drop volume V_0 [36, 37], $\alpha > 0$ a growth rate, $V_t = \int \phi^2 dv$ the drop volume at time t and dv an infinitesimally small volume element. The Lagrangian multiplier is given by $f_\ell = -\phi\phi_g\phi_s$, with $\phi_g = 1 - \phi_s - \phi$ owing to mass conservation. For more information about the Lagrangian multiplier, we refer the reader to the original literature [38,39]. The wall contribution, taken from [40], is given by

$$f_w = \phi(\phi - 1) |\mathbf{n}| \cos(\gamma) - \xi^2 \nabla\phi \cdot \nabla\phi_s, \quad (2.15)$$

with $\mathbf{n} = \xi \nabla\phi_s$, the wall-normal vector field. Because the free energy E never appears in the implementation, its formulation has deliberately been omitted. Only its functional derivative, appearing in Equation 2.12, is here relevant. The individual concentration field associated with each surface mesh, or prism, representing the structural net is given by

$$\phi_p = \frac{1}{2} \left[1 - \tanh \left(\frac{d}{\xi} \right) \right], \quad (2.16)$$

where $d(\mathbf{x})$ is the shortest signed distance from the point \mathbf{x} to the sharp prism boundary. The distance d is calculated using the pseudo-normal method [41], which works well for closed, non-self-intersecting and manifold surface meshes, as is the case here. From this, the total concentration field associated with the structural net ensues as

$$\phi_s = \sum \phi_p. \quad (2.17)$$

For the special case, in which the liquid only co-exists with the gas, that is $\phi_s = 0$, Equation 2.13 reduces to $\delta E/\delta\phi = 4\phi(\phi - 1)(\phi - 1/2) - \xi^2 \nabla^2 \phi$. In a one dimensional space, it can be analytically shown, that the solution to $\delta E/\delta\phi = 0$ is $\phi(x) = 1/2 - \tanh(x/\xi)/2$ [42], which exactly corresponds to the mathematical expression in Equation 2.16. Equation 2.12 is integrated in time using an explicit first-order forward method. Its advection term $\mathbf{u} \cdot \nabla\phi$ is discretized in space using a first-order upwind scheme. The Laplacian operator (∇^2) in Equation 2.13 and the gradient

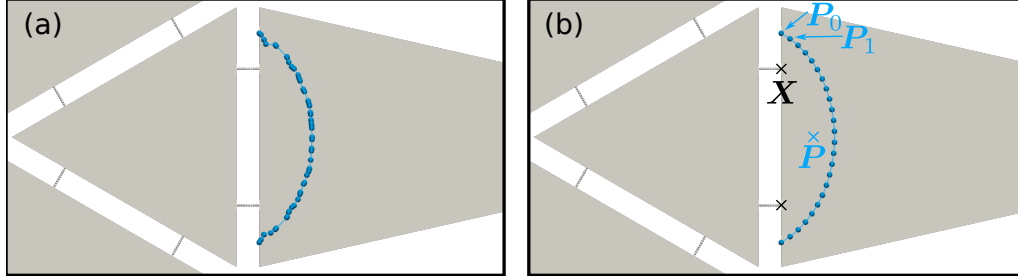


Figure 5. Original (a) and smoothed (b) three-phase contact line obtained by intersecting the structural net side with the drop.

operators (∇) in Equation 2.15 are discretized via second order schemes. The reference surface tension force is hereafter given by

$$F_c = \gamma R_0, \quad (2.18)$$

where R_0 is the equivalent drop radius previously defined.

(c) Coupling

Assuming the triangular sides have negligible mass and inertia compared to the drop, the model is closed when the surface tension force \mathbf{F}_e and torque \mathbf{T}_e acting on the last bead of each hinge are known. These act as external term in Equations 2.7-2.8. There exist various methods to estimate \mathbf{F}_e and \mathbf{T}_e . We cite for instance the continuous force model [43,44]. We here adopt another strategy based on intersecting the sharp interface of the drop with the structural net. First, the marching cubes method [29] is used to determine a tessellated surface mesh of the drop from the smooth concentration field ϕ . We are free to choose any iso-value for ϕ . A natural candidate would be $\phi = 0.5$. Our simulations have however shown, that the drop iso-surface does not always intersect with the triangular side for high contact angle, typically $\gamma > 120^\circ$. A small distance, typically one grid spacing δx , may separate the drop iso-surface from the surface mesh representing the triangular side. A simple, yet effective work around, consists in selecting a slightly lower iso-value, in this case, $\phi = 0.4$. Second, the geometrical intersection between the surface meshes representing the drop and the top surface of each triangular side are performed, resulting in a first set of polylines representing the three-phase contact lines. Because of the tessellation, the contact line is not smooth. Therefore, a new polyline $\{\mathbf{P}_i\}$ is determined by approximating it with a spline [45]. Figure 5 shows the smooth redistribution of the points forming the three-phase contact line on the triangular side. The calculation of the wall-normal surface tension force is relatively straightforward. It is given by

$$\mathbf{F}_e = \frac{1}{2} \left(\sum |\mathbf{P}_{i+1} - \mathbf{P}_i| \right) \sin(\gamma) \mathbf{n}. \quad (2.19)$$

With \mathbf{P} the barycentre of the tree-phase contact line $\{\mathbf{P}_i\}$ and \mathbf{X} the last bead position, whose index has been dropped, the external torque is given by

$$\mathbf{T}_e = \mathbf{F}_e \times (\mathbf{P} - \mathbf{X}), \quad (2.20)$$

We recall that that each triangular side is pinned to the last bead of the hinge, whose position \mathbf{X} and velocities \mathbf{V} and $\boldsymbol{\Omega}$ are known. The velocity of each triangular side hence converts to an individual Eulerian field $\mathbf{u}_p = \mathbf{V} + \boldsymbol{\Omega} \times \mathbf{r}$, where $\mathbf{r} = \mathbf{x} - \mathbf{X}$. Finally, the total velocity in Equation 2.12 is given by $\mathbf{u} = \sum \phi_p \mathbf{u}_p$.

For the implementation of the model, ingredients from various independent sources were used. To solve the advection Equation 2.12, the “PETSc” library [46], which comes with a series

of data structures and routines for solving partial differential equations on high performance computer, is used. For operations on the tessellated objects, that are the calculation of the shorted distance to the wall (Equation 2.16) and the determination of the three-phase contact line by intersecting two tessellated mesh surfaces, the “libigl” library [28] is used. For smoothing of the three-phase contact line, the “fitpack” library [47] is used. The presented method has been implemented using the Message Passing Interface for enhanced performance. In an engineering context, the model, as will be shown later, performs well and shows a relatively good performance in terms of accuracy and computational time. The source code along with the raw data presented in the following have been made available.

3. Results

(a) Validation

First, the hinge model is validated. A hinge, composed of $N_b = 10$ beads, is initially set in horizontal position and has its left extremity fixed. The position and velocity of the first bead is zero, that is $\mathbf{X}_0 = \mathbf{0}$, $\mathbf{V}_0 = \mathbf{0}$ and $\mathbf{\Omega}_0 = \mathbf{0}$. On the last bead, that is the right extremity of the hinge, an external force pointing downwards acts as $\mathbf{F}_e = -F_e \mathbf{e}_y$. The vertical deflection δ , obtained after an equilibrium state is reached, is calculated at the hinge extremity. Figure 6 shows the deflection δ as a function of the external load F_e , that we normalize with the reference structural force given in Equation 2.11. In the small-deflection region, which we define for $F_e/F_s < 1$ based on the results, the vertical deflection increases linearly with the external load as

$$\frac{\delta}{\ell} = \frac{F_e}{3F_s}. \quad (3.1)$$

The analytical solution related to the large-deflection is provided in [31]. With a number of beads set to ten, the match in terms of bending between the simulation data and the theory is excellent for both the small and large structural deformations.

Second, we perform a mesh independence study for the validation of the three-phase contact line model. To this end, a drop is initially placed on the top surface of a rectangular thin template. The mobile sides along with the hinges are here left out. The drop is initialized to a hemisphere with volume V_0 . The contact angle, γ , is varied from 20 to 140°. The simulations are performed in a cubic domain discretized into 100^3 , 150^3 and 200^3 grid points. The interfacial thickness in Equation 2.16, is hence gradually decreased from ξ to $\xi/2$, to $\xi/3$. Figure 7 shows the magnitude of the surface tension force F_e , calculated along the three-phase contact line using Equation 2.19, against the contact angle. The orange line corresponds to the theoretical solution, which assumes, that the drop at equilibrium takes the shape of a spherical cap [48,49]. In the intermediate region, $30^\circ < \gamma < 120^\circ$, the agreement between simulation and theory is relatively good. With a contact angle lower than or equal to $\gamma \leq 20^\circ$, the drop significantly flattens and, in many cases, reaches the template boundaries. That is why the simulation points may significantly deviate from the theoretical line. Beyond, that is in the region where strong to extreme dewetting occurs, deviation is also observed. In this upper interval, the three-phase contact line is generally short. Any small error in intersecting the drop iso-surface with the thin template results in relatively strong deviations. The increasing errors with decreased length of the three-phase contact line is reflected in Figure 7.

(b) Folding

Below the submillimetric scale, the surface tension force prevails by several orders of magnitude over the buoyancy and hydrostatic forces [25]. These contributions can hence be safely neglected. The key parameter in this study is the elasto-capillary number, defined as the ratio of the reference

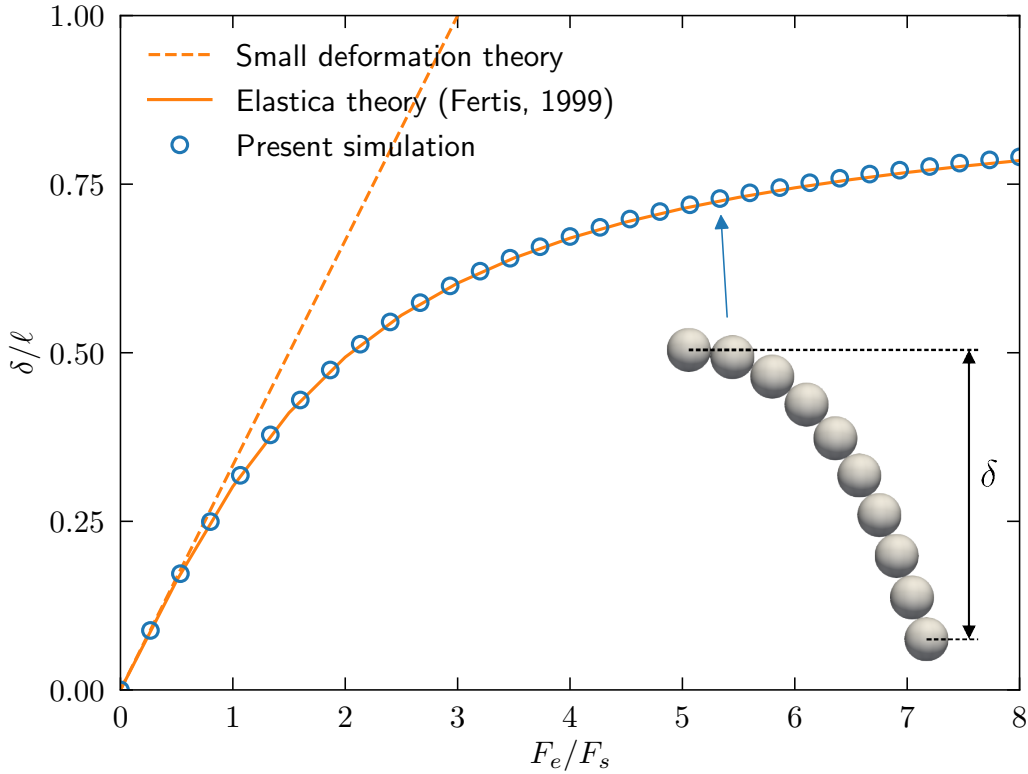


Figure 6. Vertical deflection δ of hinge composed of ten beads against external load F_e . The denominator F_s in the abscissa is the reference structural force. ℓ is the hinge length.

surface tension force to the reference structural force. It is here given by

$$Ec = \frac{F_c}{F_s}. \quad (3.2)$$

Low deformation of the hinge associated with partial encapsulation of the drop is, according to Figure 6 expected for $Ec < 1$. We further introduce the Weber and the Peclet numbers as $We = \rho U^2 \xi / \gamma$ and $Pe = \tau_d U / \xi$, where ρ is the material density of the hinge and U a reference velocity, which could for instance be the terminal velocity of the drop in the air. We also set $\xi = \Delta$, the grid spacing. Unless otherwise stated, we set $We = 1$ and $Pe = 1$. To obtain fast and stable transient simulations, the bead mass along with the diagonal components of the moment of inertia matrix are set to $m/(\rho \xi^3) = 1$ and $I/(\rho \xi^5) = 1$. We stress, that the Weber and the Peclet numbers play a secondary role and only affect the transient folding dynamics. They do not affect the final steady-state configuration. One primary interest lies here in determining the critical elasto-capillary number \tilde{Ec} , at which the transition from partial to full drop encapsulation occurs. The response time related to the material damping is set to $\tau_b \xi / U = 0.05$, thereby ensuring overdamped structural dynamics and hence shorter simulation time. In the following, we choose a cubic Eulerian domain made of 150^3 nodes.

To quantitatively discuss the results, we introduce the folding angle α between the base and the triangular side. It is illustrated in Figure 8. The subscript in α_m denotes the maximum folding angle, which corresponds to full drop encapsulation, that is when the shortest distance between two adjacent sides fall below the initial gap length (ℓ). Figure 9 illustrates the folding angle as a function of time for the structural net with a square base, that is $N = 4$. The time abscissa is made non-dimensional with the denominator $t_0 = 50 \xi / U$. At time $t/t_0 = 0$, the folding angle is zero.

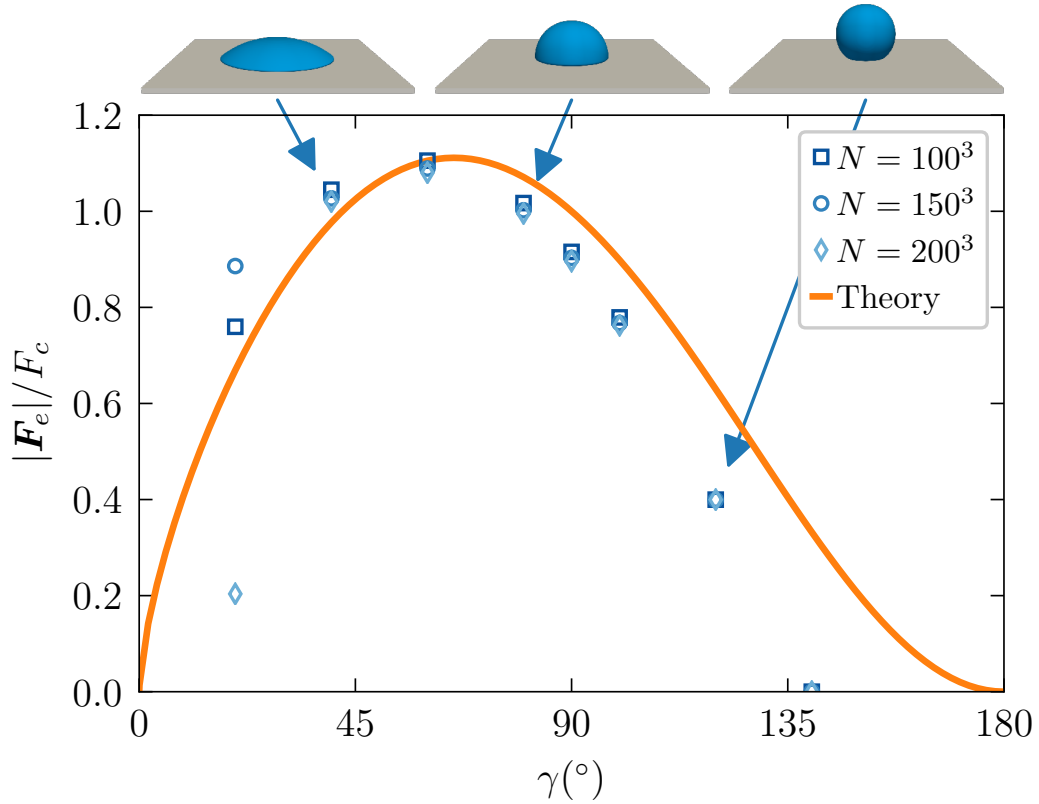


Figure 7. Surface tension force $|F_e|$ acting on a flat template against contact angle γ . The reference force is $F_0 = \gamma R_0$, where R_0 is the radius of the hemisphere obtained for $\gamma = 90^{\circ}$.

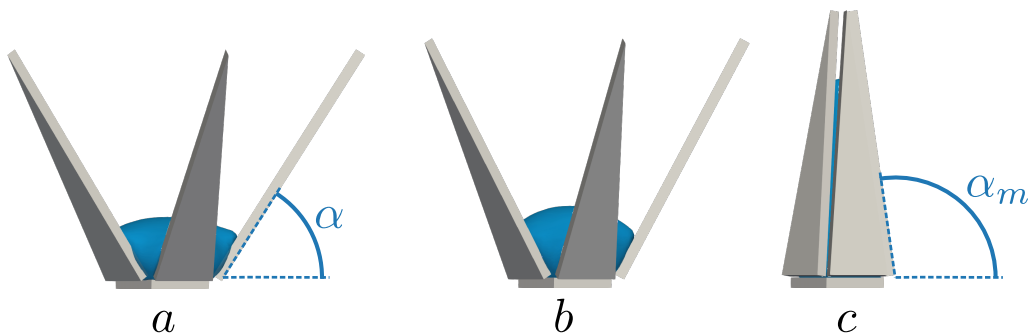


Figure 8. Partial folding and complete folding obtained at equilibrium. In a, the contact angle is set to $\gamma = 70^{\circ}$ and, in b-c, it is set to $\gamma = 90^{\circ}$. The elasto-capillary number is set to $Ec = 1.5$ in a-b and 4 in c. Because of the projection into a two-dimensional plane, only three sides of the structural net are seen. In reality, there are $N = 5$ triangular sides. The hinges are not shown.

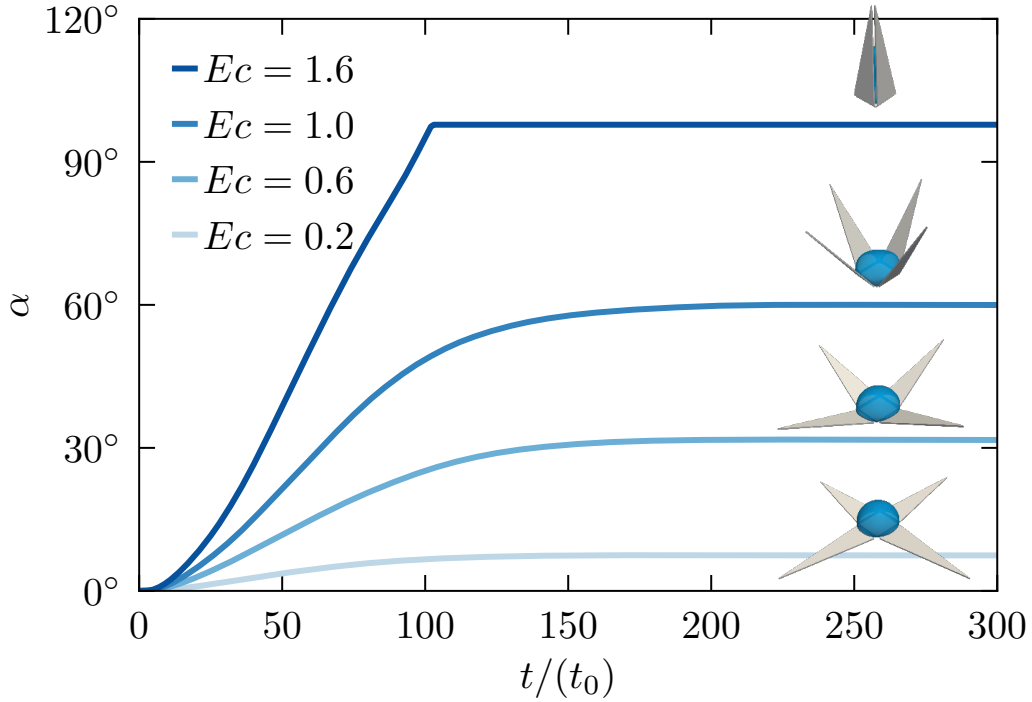


Figure 9. Folding angle (α) as a function of time. The structural net has a square base, that is $N = 4$. Ec is the elasto-capillary number.

Irrespective of the elasto-capillary number, the folding angle smoothly increases until it reaches an equilibrium $\alpha(t \rightarrow \infty) = \alpha_\infty$. We select the data obtained elasto-capillary numbers ranging from $Ec = 0.1$ to 1.6 . With $Ec = 0.1, 0.6$ and 1.0 , the encapsulation is only partial and the equilibrium folding angle equals $\alpha_\infty = 30^\circ, 58^\circ$ and 100° , respectively. With $Ec = 1.6$, a full encapsulation occurs and the folding angle is eventually capped by its maximum, which equals $\alpha_m \approx 98^\circ$. In theory, that is when the gap is null, the maximum folding angle is $\pi - \tan^{-1}(h/a)$. For $N = 3$ and $N = 7$, the maximum theoretical folding angle is 97.3° and 98.1° . A further strength of the model lies in the fact, that a temporal investigation of the folding in terms of force balance is possible. At submillimetric scale and especially during the transient, force measurement remains an experimentally difficult task to perform. With our model, the surface tension force can be precisely determined as a function of time. This is shown in Figure 10 for $Ec = 4$ and all structural nets. Irrespective of the number of sides N , the magnitude of the surface tension force increases with time until it reaches its maximum capping value α_m . A local decrease in the force is observed and occurs because the three-phase contact line is no longer continuous. A portion of the drop extends on the thin extrusion of the triangular sides, and so, the normal component of the surface tension force decreases. The results, shown in Figures 8-9, suggest that a critical elasto-capillary number exists, at which the transition from partial to full drop encapsulation occurs. To determine this transition, the equilibrium folding angle α_∞ obtained under constant Ec is shown in Figure 11. Irrespective of the number of sides N , the equilibrium folding angle increases until it reaches the plateau. To determine the transition from partial to full encapsulation, we approximate with a quadratic function of the form $\tilde{\alpha}_\infty = a_0 Ec + a_1 Ec^2$ the data points satisfying $\alpha_\infty < \alpha_m$. The coefficients a_0 and a_1 are determined with a best-fit algorithm based on the least square method. The solution to the equation, $\tilde{\alpha}_\infty(Ec) = \alpha_m$, is then used to determine the critical elasto-capillary number \tilde{Ec} . An annotation to the transition is shown in the figure 11. An increase in the number

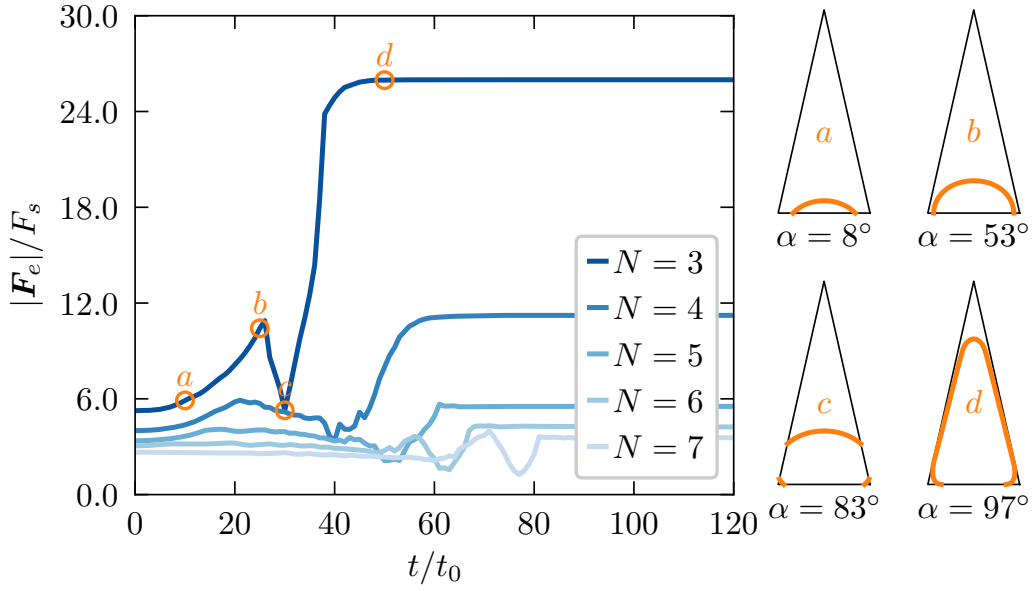


Figure 10. Capillary force against time determined for $E_c = 4$. The three phase contact line is shown at selected times, labelled a-d. F_s is the reference structural force and N the number of triangular sides in the structural net.

of sides results in a greater critical number $\tilde{E}c$. According to Equation 2.2, this is to be expected. With increasing N , the triangular sides become narrower, that is s decreases. This in-turn leads to a shorter contact line and hence to a lower surface tension force driving the folding process. To better illustrate this trend, the critical elasto-capillary number is shown in Figure 12 against the number of sides N for the contact angles $\gamma = 70^\circ$ and 90° . It is found, that the critical elasto-capillary follows a linear trend with increasing number of sides N in the structural net. We also find, that a lower contact angle, that is a drop with higher affinity to the template, does not necessarily trigger encapsulation at lower $\tilde{E}c$. With a stronger affinity to the structural net, the drop extends on the thin extruded sides and so, the normal component of the surface tension force is reduced.

4. Conclusions

In conclusion, we have introduced a numerical framework that combines structural and surface-energy minimization models to simulate complex nano- and micro-origami self-folding processes in three dimensions. Our model involves a liquid drop that induces spontaneous folding and dynamic deformation of the structural net. As application, we have simulated the self-folding of two-dimensional templates into pyramidal micro-structures and determined the transition from partial to full drop encapsulation. Advantages of the model include a limited number of arbitrary user-defined parameters and the incorporation of time-derivative terms addressing unsteady dynamics. In the future, the model will be extended to consider more arbitrary structural nets, for example with an asymmetry. Evaporation will also be considered, because in the submillimeter scale, it can occur rapidly. This can be done in a relatively easy way by changing the tuning the parameter β in Equation 2.14.

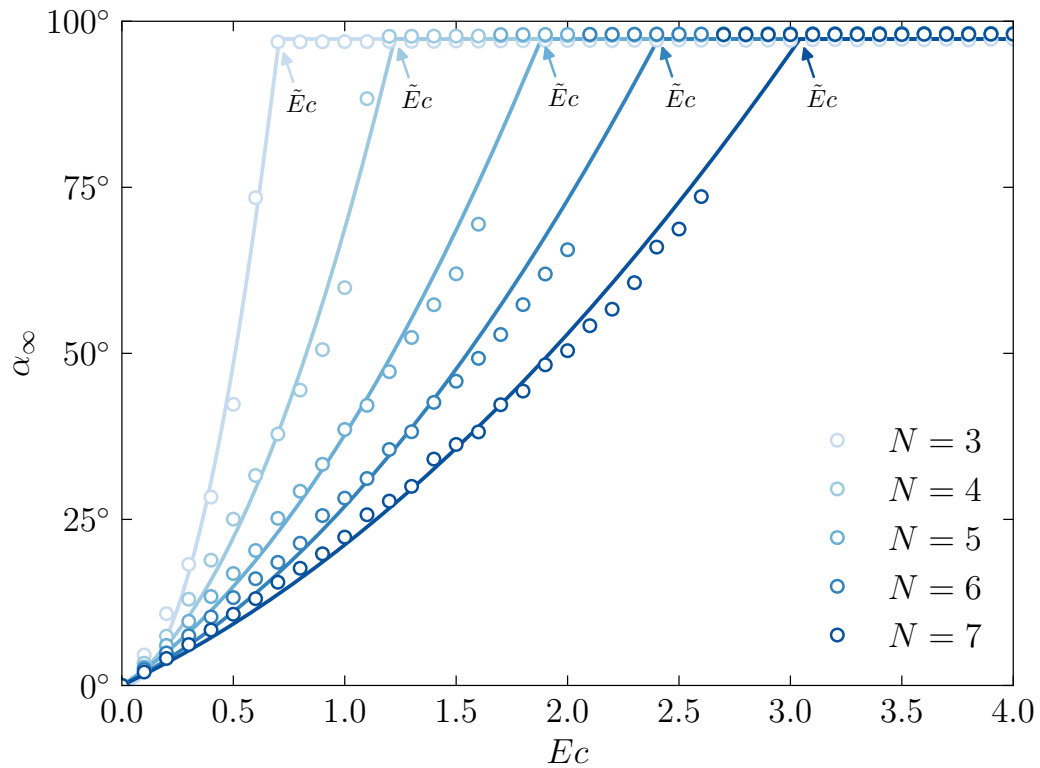


Figure 11. Equilibrium folding angle $\alpha_\infty = \alpha(t \rightarrow \infty)$ against elasto-capillary number Ec . \tilde{Ec} is the critical value, at which full encapsulation occurs. The quadratic curves $\tilde{\alpha}_\infty(Ec)$ are best fitted to the simulation data. N is the number of triangular sides.

Acknowledgments

This work was supported by the German Research Foundation (Deutsche Forschungsgemeinschaft) under the project numbers 492454247 and 419981939.

Funding

This work was supported by the German Research Foundation (Deutsche Forschungsgemeinschaft) under the project numbers 492454247 and 4199

References

1. Py C, Reverdy P, Doppler L, Bico J, Roman B, Baroud CN. 2007 Capillary origami: spontaneous wrapping of a droplet with an elastic sheet. *Physical Review Letters* **98**, 156103. ([10.1103/PhysRevLett.98.156103](https://doi.org/10.1103/PhysRevLett.98.156103))
2. Roman B, Bico J. 2010 Elasto-capillarity: deforming an elastic structure with a liquid droplet. *Journal of Physics: Condensed Matter* **22**, 493101. ([10.1088/0953-8984/22/49/493101](https://doi.org/10.1088/0953-8984/22/49/493101))
3. Bae J, Ouchi T, Hayward RC. 2015 Measuring the elastic modulus of thin polymer sheets by elastocapillary bending. *ACS Applied Materials & Interfaces* **7**, 14734–14742. ([10.1021/acsami.5b02567](https://doi.org/10.1021/acsami.5b02567))
4. Bico J, Reyssat É, Roman B. 2018 Elastocapillarity: when surface tension deforms elastic solids. *Annual Review of Fluid Mechanics* **50**, 629–659. ([10.1146/annurev-fluid-122316-050130](https://doi.org/10.1146/annurev-fluid-122316-050130))

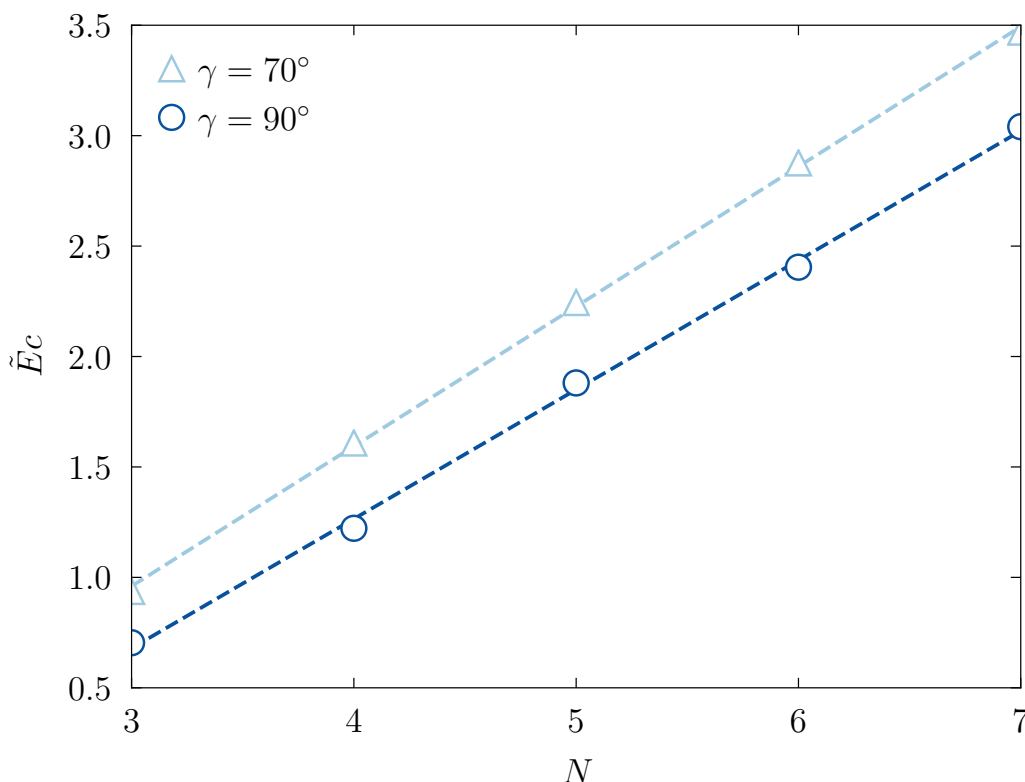


Figure 12. Critical elasto-capillary number $\tilde{E}c$, at which full drop encapsulation occurs. The dashed lines are a guide for the eye and aim at showing the linear dependency with the number of sides.

5. Kwok KS, Huang Q, Mastrangeli M, Gracias DH. 2020 Self-folding using capillary forces. *Advanced Materials Interfaces* **7**, 1901677. ([10.1002/admi.201901677](https://doi.org/10.1002/admi.201901677))
6. Reis PM, Hure J, Jung S, Bush JWM, Clanet C. 2010 Grabbing water. *Soft Matter* **6**, 5705–5708. ([10.1039/C0SM00895H](https://doi.org/10.1039/C0SM00895H))
7. Syms R, Yeatman E, Bright V, Whitesides G. 2003 Surface tension-powered self-assembly of microstructures - the state-of-the-art. *Journal of Microelectromechanical Systems* **12**, 387–417. ([10.1109/JMEMS.2003.811724](https://doi.org/10.1109/JMEMS.2003.811724))
8. Guo X, Li H, Ahn BY, Duoss EB, Hsia KJ, Lewis JA, Nuzzo RG. 2009 Two- and three-dimensional folding of thin film single-crystalline silicon for photovoltaic power applications. *Proceedings of the National Academy of Sciences* **106**, 20149–20154. ([10.1073/pnas.0907390106](https://doi.org/10.1073/pnas.0907390106))
9. Zhang Y, Zhang F, Yan Z, Ma Q, Li X, Huang Y, Rogers JA. 2017 Printing, folding and assembly methods for forming 3D mesostructures in advanced materials. *Nature Reviews Materials* **2**, 17019. ([10.1038/natrevmats.2017.19](https://doi.org/10.1038/natrevmats.2017.19))
10. Demaine ED, O'Rourke J. 2007 *Geometric folding algorithms: linkages, origami, polyhedra*. Cambridge University Press. ([10.1017/CBO9780511735172](https://doi.org/10.1017/CBO9780511735172))
11. Pandey S, Ewing M, Kunas A, Nguyen N, Gracias DH, Menon G. 2011 Algorithmic design of self-folding polyhedra. *Proceedings of the National Academy of Sciences* **108**, 19885–19890. ([10.1073/pnas.111085710](https://doi.org/10.1073/pnas.111085710))
12. Kaplan R, Klobusicky J, Pandey S, Gracias DH, Menon G. 2014 Building polyhedra by self-assembly: theory and experiment. *Artificial Life* **20**, 409–439.
13. Twohig T, Croll AB. 2021 Adhesion directed capillary origami. *Soft Matter* **17**, 9170–9180. ([10.1039/D1SM01142A](https://doi.org/10.1039/D1SM01142A))
14. Ionov L. 2011 Soft microorigami: self-folding polymer films. *Soft Matter* **7**, 6786–6791. ([10.1039/C1SM05476G](https://doi.org/10.1039/C1SM05476G))
15. Fernandes R, Gracias DH. 2012 Self-folding polymeric containers for encapsulation and

- delivery of drugs. *Advanced Drug Delivery Reviews* **64**, 1579–1589. Emerging micro- and nanotechnologies for the development of novel drug delivery devices and systems ([10.1016/j.addr.2012.02.012](https://doi.org/10.1016/j.addr.2012.02.012))
16. Bolanos Quinones VA, Zhu H, Solovev AA, Mei Y, Gracias DH. 2018 Origami biosystems: 3D assembly methods for biomedical applications. *Advanced Biosystems* **2**, 1800230. ([10.1002/adbi.201800230](https://doi.org/10.1002/adbi.201800230))
 17. Patra N, Wang B, Král P. 2009 Nanodroplet activated and guided folding of graphene nanostructures. *Nano Letters* **9**, 3766–3771. PMID: 19852466 ([10.1021/nl9019616](https://doi.org/10.1021/nl9019616))
 18. Leong TG, Lester PA, Koh TL, Call EK, Gracias DH. 2007 Surface tension-driven self-folding polyhedra. *Langmuir* **23**, 8747–8751. PMID: 17608507 ([10.1021/la700913m](https://doi.org/10.1021/la700913m))
 19. Brakke KA. 1992 The Surface Evolver. *Experimental Mathematics* **1**, 141–165. ([10.1080/10586458.1992.10504253](https://doi.org/10.1080/10586458.1992.10504253))
 20. van Honschoten JW, Berenschot JW, Ondarçuhu T, Sanders RGP, Sundaram J, Elwenspoek M, Tas NR. 2010 Elastocapillary fabrication of three-dimensional microstructures. *Applied Physics Letters* **97**, 014103. ([10.1063/1.3462302](https://doi.org/10.1063/1.3462302))
 21. Legrain A, Janson TG, Berenschot JW, Abelman L, Tas NR. 2014 Controllable elastocapillary folding of three-dimensional micro-objects by through-wafer filling. *Journal of Applied Physics* **115**, 214905. ([10.1063/1.4878460](https://doi.org/10.1063/1.4878460))
 22. de Langre E, Baroud C, Reverdy P. 2010 Energy criteria for elasto-capillary wrapping. *Journal of Fluids and Structures* **26**, 205–217. ([10.1016/j.jfluidstructs.2009.10.004](https://doi.org/10.1016/j.jfluidstructs.2009.10.004))
 23. Brubaker N, Lega J. 2016 Two-dimensional capillary origami. *Physics Letters A* **380**, 83–87. ([10.1016/j.physleta.2015.09.002](https://doi.org/10.1016/j.physleta.2015.09.002))
 24. Elettro H, Grandgeorge P, Neukirch S. 2017 Elastocapillary coiling of an elastic rod inside a drop. *Journal of Elasticity* **127**, 235–247. ([10.1007/s10659-016-9611-4](https://doi.org/10.1007/s10659-016-9611-4))
 25. Neukirch S, Antkowiak A, Marigo JJ. 2013 The bending of an elastic beam by a liquid drop: a variational approach. *Proceedings of the Royal Society A: Mathematical, Physical and Engineering Sciences* **469**, 20130066. ([10.1098/rspa.2013.0066](https://doi.org/10.1098/rspa.2013.0066))
 26. Bosi F, Misseroni D, Dal Corso F, Bigoni D. 2015 Self-encapsulation, or the ‘dripping’ of an elastic rod. *Proceedings of the Royal Society A: Mathematical, Physical and Engineering Sciences* **471**, 20150195. ([10.1098/rspa.2015.0195](https://doi.org/10.1098/rspa.2015.0195))
 27. Brubaker ND, Lega J. 2016 Capillary-induced deformations of a thin elastic sheet. *Philosophical Transactions of the Royal Society A: Mathematical, Physical and Engineering Sciences* **374**, 20150169. ([10.1098/rsta.2015.0169](https://doi.org/10.1098/rsta.2015.0169))
 28. Jacobson A, Panozzo D et al.. 2018 libigl: A simple C++ geometry processing library. <https://libigl.github.io/>.
 29. Lorensen WE, Cline HE. 1987 Marching Cubes: A High Resolution 3D Surface Construction Algorithm. *SIGGRAPH Comput. Graph.* **21**, 163–169. ([10.1145/37402.37422](https://doi.org/10.1145/37402.37422))
 30. André D, Iordanoff I, Charles JL, Néauport J. 2012 Discrete element method to simulate continuous material by using the cohesive beam model. *Computer Methods in Applied Mechanics and Engineering* **213–216**, 113–125. ([10.1016/j.cma.2011.12.002](https://doi.org/10.1016/j.cma.2011.12.002))
 31. Fertis D. 1993 *Nonlinear mechanics*. Taylor & Francis.
 32. Lecrivain G, Grein TBP, Yamamoto R, Hampel U, Taniguchi T. 2020 Eulerian/Lagrangian formulation for the elasto-capillary deformation of a flexible fibre. *Journal of Computational Physics* **409**, 109324. ([10.1016/j.jcp.2020.109324](https://doi.org/10.1016/j.jcp.2020.109324))
 33. Guo Y, Wassgren C, Curtis JS, Xu D. 2018 A bonded sphero-cylinder model for the discrete element simulation of elasto-plastic fibers. *Chemical Engineering Science* **175**, 118–129. ([10.1016/j.ces.2017.09.029](https://doi.org/10.1016/j.ces.2017.09.029))
 34. Aihara S, Takaki T, Takada N. 2019 Multi-phase-field modeling using a conservative Allen–Cahn equation for multiphase flow. *Computers & Fluids* **178**, 141–151. ([10.1016/j.compfluid.2018.08.023](https://doi.org/10.1016/j.compfluid.2018.08.023))
 35. Araki T, Tanaka H. 2006 Wetting-induced depletion interaction between particles in a phase-separating liquid mixture. *Physical Review E* **73**, 061506. ([10.1103/PhysRevE.73.061506](https://doi.org/10.1103/PhysRevE.73.061506))
 36. Nonomura M. 2012 Study on Multicellular Systems Using a Phase Field Model. *PLOS ONE* **7**, 1–9. ([10.1371/journal.pone.0033501](https://doi.org/10.1371/journal.pone.0033501))
 37. Lavoratti TC, Heitkam S, Hampel U, Lecrivain G. 2021 A computational method to simulate mono- and poly-disperse two-dimensional foams flowing in obstructed channel. *Rheologica Acta* **60**, 587–601. ([10.1007/s00397-021-01288-y](https://doi.org/10.1007/s00397-021-01288-y))
 38. Lee HG, Kim J. 2008 A second-order accurate non-linear difference scheme for the N - component Cahn–Hilliard system. *Physica A: Statistical Mechanics and its Applications* **387**,

- 4787–4799. ([10.1016/j.physa.2008.03.023](https://doi.org/10.1016/j.physa.2008.03.023))
39. Boyer F, Lapuerta C, Minjeaud S, Piar B, Quintard M. 2010 Cahn–Hilliard/Navier–Stokes model for the simulation of three-phase flows. *Transport in Porous Media* **82**, 463–483. ([10.1007/s11242-009-9408-z](https://doi.org/10.1007/s11242-009-9408-z))
 40. Yang J, Kim J. 2020 A phase-field method for two-phase fluid flow in arbitrary domains. *Computers & Mathematics with Applications* **79**, 1857–1874. ([10.1016/j.camwa.2019.10.008](https://doi.org/10.1016/j.camwa.2019.10.008))
 41. Baerentzen J, Aanaes H. 2005 Signed distance computation using the angle weighted pseudonormal. *IEEE Transactions on Visualization and Computer Graphics* **11**, 243–253. ([10.1109/TVCG.2005.49](https://doi.org/10.1109/TVCG.2005.49))
 42. Shinto H, Miyahara M, Higashitani K. 1999 Evaluation of interaction forces between macroparticles in simple fluids by molecular dynamics simulation. *Journal of Colloid and Interface Science* **209**, 79–85. ([10.1006/jcis.1998.5870](https://doi.org/10.1006/jcis.1998.5870))
 43. Brackbill J, Kothe D, Zemach C. 1992 A continuum method for modeling surface tension. *Journal of Computational Physics* **100**, 335–354. ([10.1016/0021-9991\(92\)90240-Y](https://doi.org/10.1016/0021-9991(92)90240-Y))
 44. Kim J. 2005 A continuous surface tension force formulation for diffuse-interface models. *Journal of Computational Physics* **204**, 784–804. ([10.1016/j.jcp.2004.10.032](https://doi.org/10.1016/j.jcp.2004.10.032))
 45. Dierckx P. 1993 *Curve and surface fitting with splines*. Oxford University Press.
 46. Balay S, Abhyankar S, Adams MF, Benson S, Brown J, Brune P, Buschelman K, Constantinescu EM, Dalcin L, Dener A, Eijkhout V, Gropp WD, Hapla V, Isaac T, Jolivet P, Karpeev D, Kaushik D, Knepley MG, Kong F, Kruger S, May DA, McInnes LC, Mills RT, Mitchell L, Munson T, Roman JE, Rupp K, Sanan P, Sarich J, Smith BF, Zampini S, Zhang H, Zhang H, Zhang J. 2022 PETSc Web page. <https://petsc.org/>.
 47. Dierckx P. 1993 FITPACK. <https://netlib.org/dierckx/>.
 48. Hu H, Larson RG. 2002 Evaporation of a sessile droplet on a substrate. *The Journal of Physical Chemistry B* **106**, 1334–1344. ([10.1021/jp0118322](https://doi.org/10.1021/jp0118322))
 49. Schmieschek S, Harting J. 2011 Contact Angle Determination in Multicomponent Lattice Boltzmann Simulations. *Communications in Computational Physics* **9**, 1165–1178. ([10.4208/cicp.201009.271010s](https://doi.org/10.4208/cicp.201009.271010s))

Ethics statement

This article did not involve human participants or animals.

Competing interests statement

The authors report no conflict of interest.

Data accessibility statement

The source code and the data that support the findings of this study will be made available in with a DOI after an embargo period, that is when the manuscript is accepted for publication.

Author contributions

GL developed the model, performed the simulation and wrote the first draft of the manuscript. PL and KZ performed the illustrative experiment. GL, KZ and UH contributed to the acquisition of the financial support for this work. All authors aided in interpreting the results and work on the manuscript.